

Be<sup>10</sup> AND U-SERIES ISOTOPES IN MANGANESE NODULES FROM THE  
CENTRAL NORTH PACIFIC

T. L. Ku, A. Omura\* and P. S. Chen

Department of Geological Sciences  
University of Southern California  
Los Angeles, California 90007

Abstract

The exponential decreases with depth of Be<sup>10</sup>, Th<sup>230</sup> and Pa<sup>231</sup> in two manganese nodules from the central North Pacific is interpreted in terms of slow growth of the nodules: at average rates of millimeters per million years. We observe in one specimen (Mn 139): Be<sup>10</sup>-based rate < Th<sup>230</sup>-based rate < Pa<sup>231</sup>-based rate. This suggests that diffusion-mixing may have modified the depth gradients of these nuclides, such that the true rate would be close to or even lower than the observed Be<sup>10</sup> rate of 1.3 mm/10<sup>6</sup>yr. Quantitative assessment using a diffusion-decay model indicates that in Mn 139, Th<sup>230</sup> and Pa<sup>231</sup> could have been subjected to diffusion-like transport with an effective diffusion coefficient of  $\sim 1 \times 10^{-8} \text{ cm}^2/\text{yr}$ . After correction for this effect, the Th<sup>230</sup> and Pa<sup>231</sup> data give a concordant rate of 1.9 mm/10<sup>6</sup>yr, about 2-3 times lower than their uncorrected values. The small and variable amounts of integrated dpm/cm<sup>2</sup> of Be<sup>10</sup>, Th<sub>ex</sub><sup>230</sup> and Pa<sub>ex</sub><sup>231</sup> found in nodules are best explained by their incorporating only a fraction of the nuclides supplied due to frequent coverage by sediments. The alternative explanation of young "exposure" ages is refutable on several grounds. Among these, we show that diffusion of nuclides required by the exposure-age concept yields depth profiles that are not of the commonly observed exponential form.

---

\*Presently at Department of Earth Sciences, Kanazawa University, Kanazawa 920, Japan.

### Introduction

The slow growth rates of deep-sea manganese nodules, by and large, have been documented by radiometric measurements. Their long-term, average rates are of the order of millimeters per million years (see Ku, 1977). This is compared with the accumulation rates of millimeters per thousand years for sediments in the nodule fields. The disparity raises the question of how nodules can escape burial by the fast depositing sediments, often leading to arguments against the validity of radiometric dating. One such argument states that the rapid exponential decrease with depth of unsupported  $\text{Th}^{230}$  and  $\text{Pa}^{231}$  found in nodule surface layers could be due to surface adsorption and diffusion of these nuclides and/or to sampling artifact resulting from the highly crenulated nodule morphology (Arrhenius, 1967; Lalou and Brichet, 1972), rather than due to radioactive decay. This reasoning is clearly unacceptable if concordant rates are obtained from the distribution of radioactive nuclides with vastly different half-lives. Such has been the case for the simultaneous measurements of  $\text{Th}^{230}$  and  $\text{Be}^{10}$  on two nodules: Zetes-3D and Tripod-2D (Bhat et al., 1973). However, the data base for this concordancy check is still considered limited. For Zetes-3D, as an example, the comparison was made based on a total of five analyses of  $\text{Th}^{230}$  and  $\text{Be}^{10}$ . The  $\text{Th}^{230}$  data were from two layers down to a depth of 0.14 mm, whereas the three analyses of  $\text{Be}^{10}$  covered the depth range of 0-13 mm; no  $\text{Pa}^{231}$  measurements were made. Recently published results of Guichard et al. (1978) show more detailed  $\text{Be}^{10}$  profiles obtained for a Mn-encrustation from the south Pacific. Comparative studies of the U and Th decay series nuclides on this same specimen are in progress (Lalou et al., 1978). We now report a similar study carried out on two manganese nodules from the central North Pacific. It was hoped that, with the more detailed measurements than previously available, we would be able to evaluate in a more rigorous way the possibility and implications of the "open system" brought about by the hypothesis of rapid growth of nodules.

### Materials Studied

The specimens taken for study are ARIES 13D and Mn 139. ARIES 13D was dredged from a terrace of a seamount in an area with rugged topography near  $20^{\circ}45'N$ ,  $173^{\circ}40'E$ . Water depths recorded during the dredging operation were 3816-2955 m. The sample is discoidal in shape and about 11 cm at its longest side. As shown in Fig. 1A, the Mn-Fe oxide coating is very asymmetrical around a nucleus of altered basaltic rock. Three layers, L1, L2, and L3, scraped parallel to the surface, are sampled from the thick side (2.2 cm) of the oxide coating. The thickness of each layer is measured at several points using calipers read to 0.05

mm. The opposite side of the coating measures only about 0.2-0.3 cm thick.

The Mn 139 nodule, recovered from a depth of 3916 m at 20°01'N, 136°36'W, is also discoid-shaped with a slightly convex (upward) bottom (see Fig. 1B, also for dimensions). It has a fairly unusual morphological appearance in that it can be divided into two parts according to the external as well as internal structures. The surface of one part is relatively smooth whereas the other part exhibits rough and knobby surfaces. The "knobs" are surface expressions of small concretions ranging from mm to 2 cm in diameter. Nodule material beneath the smooth surface, similar to that of ARIES 13D, is uniform and almost structureless. The nucleus material is inconspicuous. As sketched in Fig. 1B, layers of various thickness, L1 through L5, are sampled from the "smooth" side. The thickness of the layers is also measured using the calipers. Before sampling of L1-L5, six thin layers (T1 through T6) have been successively scraped

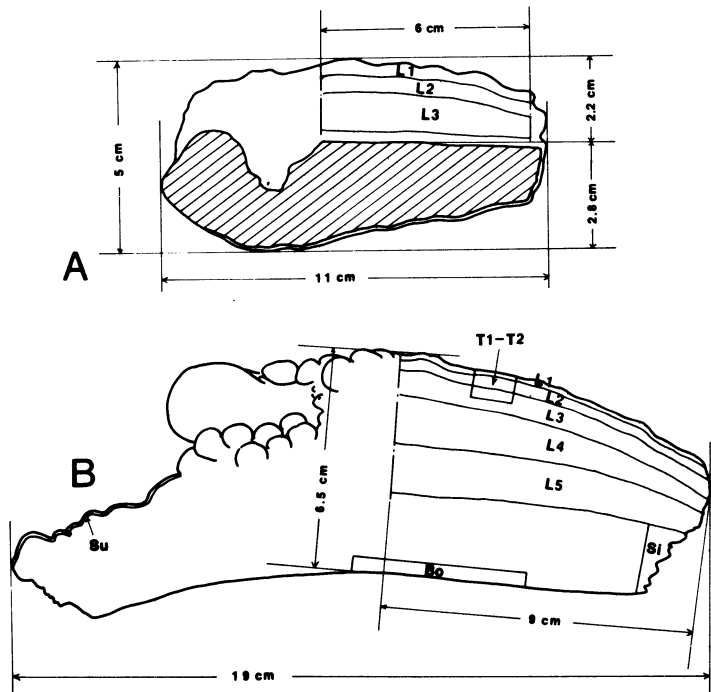


Fig. 1. Sketches of ARIES 13D (A) and a side-view of Mn 139 (B) showing the dimensions and sampled areas. Note the morphological difference in two parts of Mn 139.

from an area of 2.25 cm<sup>2</sup> from the top surface down to a depth of about 7 mm (Fig. 1B). The thickness of each of these thin layers is estimated by the method of Bender *et al.* (1966), taking the density of nodule material as 2 gr/cm<sup>3</sup>.

Three more samples, designated as Bo, Su, and Si, are taken from Mn 139 for analysis. Their approximate position and thickness are shown in Fig. 1B and Table 1, respectively.

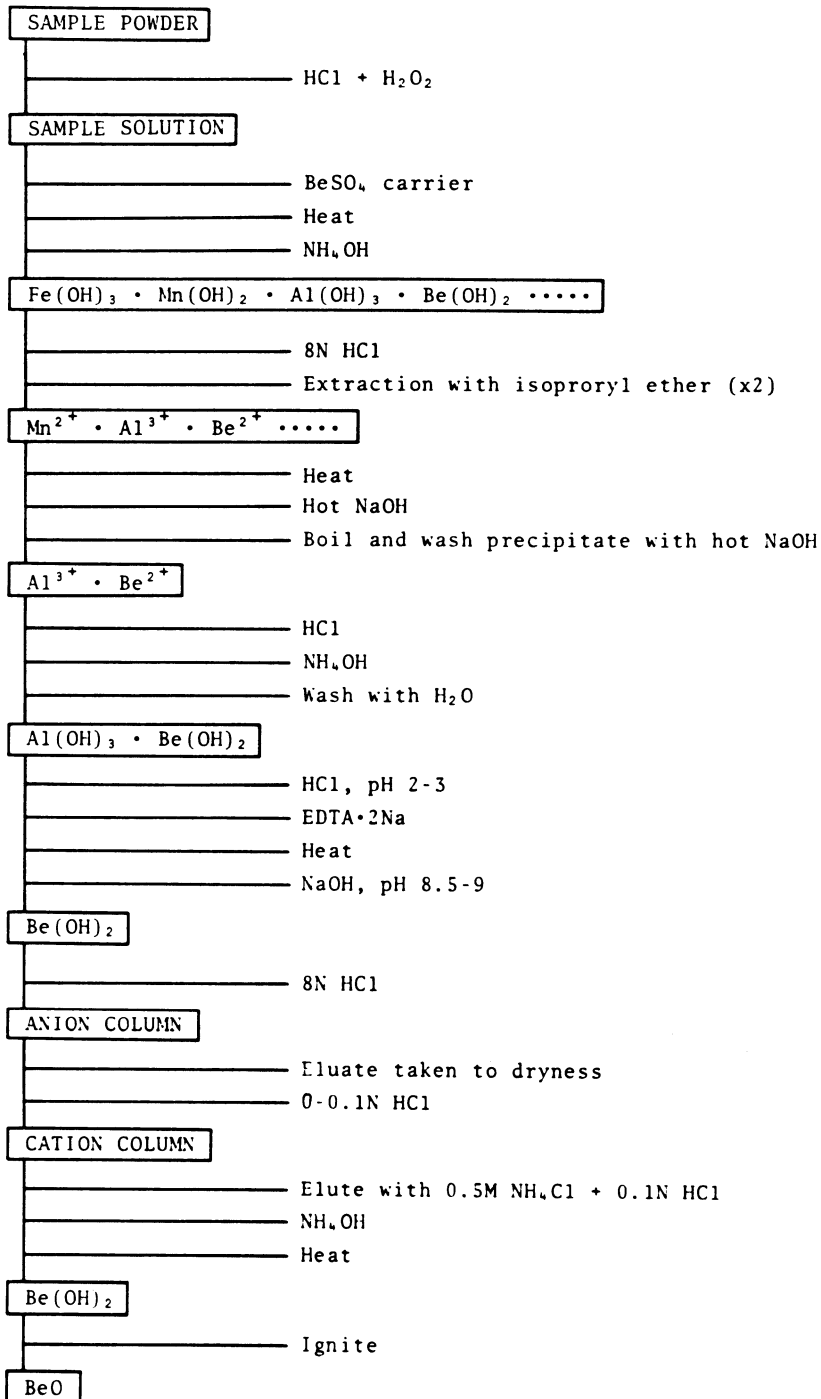
### Experimental

The sampled nodule material is pulverized to powder form, homogenized, and dried at 110°C before analysis.

Figure 2 gives a flow diagram for Be<sup>10</sup> analysis. The sample powder is first dissolved in a HCl-H<sub>2</sub>O<sub>2</sub> mixture. The solution is centrifuged. The residue is washed with water and the washings added to the solution, to which a BeSO<sub>4</sub> carrier-yield tracer (30-60 mg BeO) is added. After heating to decompose H<sub>2</sub>O<sub>2</sub>, the solution is made to 8N HCl from which iron is removed by extraction with isopropyl ether. Removal of manganese is accomplished by boiling the solution with NaOH. The NaOH washings of the precipitate and the supernatant are combined, from which hydroxides of Al and Be are precipitated with the addition of first HCl, and then NH<sub>4</sub>OH. The hydroxides are redissolved in HCl to a pH of 2-3. At this point, a 20% EDTA·2Na solution is added as a masking agent for Al. The solution is heated and its pH raised to 8.5-9 with NaOH. The Be(OH)<sub>2</sub> precipitate thus formed is dissolved in HCl to a strength of 8N.

Anion- and cation- exchange techniques are performed afterwards for Be purification. The 8N HCl sample solution is passed through an anion column (Dowex 1x8, 100-200 mesh) prepared with 1 column volume (cv) of 0.1N HCl and 2 cv of 8N HCl. The column is washed with 3 cv of 8N HCl; the washing and the effluent are combined and evaporated to dryness. Beryllium is taken up in 0.1N HCl and the solution is then passed through a cation column (Dowex 50x8, 200-400 mesh) prepared successively with 1 cv of 0.5N HCl, 4 cv of 4N HCl and 2 cv of H<sub>2</sub>O. After the column is washed with 2 cv of H<sub>2</sub>O and 15 cv of 0.5M oxalic acid, Be is desorbed by elution with 10 cv of a mixture of 0.5N NH<sub>4</sub>OH and 0.1N HCl.

For counting of the purified Be, it is precipitated as Be(OH)<sub>2</sub> and then ignited to form BeO. The latter is powdered and wetted before being transferred onto the lucite source holder of the beta detector, dried under an infrared lamp, and covered with mylar (0.84 mg/cm<sup>2</sup>). The source holder provides an area of 3.9 cm<sup>2</sup> for counting. For each sample mount, the beta activity of Be<sup>10</sup> is counted twice, usually about 1½ months apart, and using two different counters. These counters are of the design of Lal and Schink (1960). "Q" gas (98.7% helium and 1.3% butane

Fig. 2. Flow diagram of Be<sup>10</sup> purification chemistry.

mixture) is used as the flowing counting gas. The backgrounds of the two counters have remained stable at  $10.4 \pm .3$  and  $13.1 \pm .6$  counts per hour respectively, throughout the 10-month period of the experiment. The counting efficiency, as checked with the four  $\text{Pb}^{210}$  standards supplied by Dr. Y. C. Chung of Scripps Institution of Oceanography, is 43% and 44% for the two counters. Correction factors for external and self absorption as well as counting efficiency are applied to the observed counting rates for obtaining the absolute disintegration rates.

A blank for  $\text{Be}^{10}$  has been measured on all the chemicals and apparatus used as in sample runs, following the procedures described above.

Methods for the measurements of uranium, thorium, and protactinium isotopes are those of Ku and Broecker (1969) with minor modifications. The common beryllium ( $\text{Be}^9$ ) is measured using atomic absorption spectrophotometry (Perkin-Elmer 305B, equipped with HGA-2100 graphite furnace).

### Analytical Results

Results of the beryllium measurements are presented in Tables 1 and 2; those of the decay series isotopes, in Tables 3 and 4. The quoted errors are standard deviations ( $1\sigma$ ) derived from counting statistics. The estimated error in the  $\text{Be}^9$  analyses is about  $\pm 5\%$ .

As the number of  $\text{Be}^{10}$  analyses reported herein almost equals those which have appeared in literature to date, an appraisal of the Table 1 data is in order. It is apparent that for the very low abundance of  $\text{Be}^{10}$  to be detected, purification of  $\text{Be}^{10}$  against the numerous possible beta-emitting contaminants is exceedingly important. The purity can be assessed via counting techniques: by checking the energy of the beta radiation using absorbers or a two-element counter. But, perhaps a more effective and straight-forward means of checking is to recount the samples after chemical repurification. The results of this test for samples of Mn 139 and the blank are listed in Table 1. Clearly, the high reproducibility of the two purification results attest to the soundness of the analytical scheme. Sample Mn 139-L1, analyzed at the very beginning of the experiment, is one exception. A third purification of the sample has been carried out and found to agree with the second. It should be noted that in repurifying the already prepared  $\text{BeO}$ , much smaller quantities of reagents are used as compared to those required during the initial Be concentration and purification steps. Hence almost negligible blank corrections (as also reflected by the "Blank" data in Table 1) are applied to the repurification results. The repurifications usually yield high chemical recovery, about 70-90%; the listed chemical yields in Table 1 refer to % recovery of

TABLE 1

Be<sup>10</sup> Analyses on Manganese Nodules ARIES 13D and Mn 139

Sample No.	Depth (mm)	Weight (g)	Residue (wt.%)	Chemical <sup>1</sup> yield (%)	Net count rate <sup>2</sup> Be <sup>10</sup> (cph)	Conc. <sup>3</sup> (dpm/kg nodule)
<b>ARIES 13D</b>						
L1	0-4.3	16.7	6.8	24.0	3.56±.47	48.9±6.5
L2	4.3-8.8	29.6	11.8	33.	3.08±.56	17.7±3.2
L3	8.8-18.2	71.1	6.3	44.0	3.21±.57	5.48±.97
<b>Mn 139</b>						
L1	0-0.8	9.22	12.2	(1)33.4 (2)21.4 (3)17.5	8.64±.63 3.80±.48 3.34±.44	171±13 114±14 121±16
L2	0.8-3.6	21.0	18.0	(1)42.9 (2)31.1	6.18±.62 4.63±.42	46.0±4.7 46.3±4.1
L3	3.6-9.4	35.5	18.2	(1)45.3 (2)37.8	3.89±.44 3.32±.41	16.4±1.9 16.3±2.1
L4	9.4-24.1	64.0	18.4	(1)48.3 (2)38.6	2.75±.43 2.18±.40	5.13±.80 4.97±.91
L5	24.1-38.4	102	17.3	(1)45.8 (2)39.9	2.06±.44 1.64±.40	2.93±.62 2.65±.65
Bo	59.1-65.0	23.3	9.7	(1)47.1 (2)41.2	0.13±.78 0.18±.31	0.75±4.50 1.16±2.00
Su	1.0	6.6	22.7	(1)51.7 (2)43.2	2.05±.39 1.49±.43	42.8±8.3 37.7±10.8
Si	0-<1.5 (irregular)	15.8	6.9	(1)44.6 (2)39.2	3.95±.41 2.95±.41	33.4±3.5 27.8±3.7
Blank	---	---	---	(1)57.0 (2)44.4	0.89±.37 0.96±.38	----- -----

1. Number in parenthesis denotes 1st purification, 2nd purification, etc.
2. Beta count rate (for samples) after correction of counter background and blank (yield-normalized).
3. The weight of nodule material is defined as that leachable by HCl-H<sub>2</sub>O<sub>2</sub>.

TABLE 2  
Be<sup>10</sup> Concentration and Be<sup>10</sup>/Be<sup>9</sup> in ARIES 13D and Mn 139

Sample No.	Be <sup>10</sup> conc. <sup>1</sup> (dpm/kg nodule)	Be <sup>9</sup> conc. (mg/kg nodule)	Be <sup>10</sup> /Be <sup>9</sup> (10 <sup>3</sup> dpm/g)
<u>ARIES 13D</u>			
L1	48.9±6.5	9.8	5.0±.7
L2	17.7±3.2	8.8	2.0±.4
L3	5.48±.97	9.0	0.62±.11
<u>Mn 139</u>			
L1	118±11	8.5	13.9±1.5
L2	46.2±3.1	8.3	5.6±.5
L3	16.4±1.4	8.4	2.0±.2
L4	5.05±.61	9.2	0.55±.07
L5	2.79±.45	9.5	0.29±.05
Bo	0.96±2.46	8.9	0.10±.25
Su	40.3±6.8	9.1	4.4±.8
Si	30.6±2.5	9.4	3.3±.3

1. For Mn 139, weighted averages of the 1st and 2nd purification results are reported here (except for layer L1, in which case the average of 2nd and 3rd purification results is used).

the originally added BeO carrier.

One can safely assume from the reproducibility that virtually all beta emitters except Be<sup>10</sup> are eliminated after the single cycle of purification steps shown in Fig. 2. This assumption has been applied to the ARIES 13D samples for which no repurifications are performed. The Be<sup>10</sup> data summarized in Table 2 for Mn 139 samples are, accordingly, weighted averages (based on counting statistics) of the two purification results.

The counters used have good stability in background and efficiency. Alternate countings of each sample mount in the two counters as mentioned earlier have given consistent results.

However, the counter backgrounds clearly constitute the dominant signal in the present analyses, and they are the limiting factor for precision as well as sensitivity.

### Discussion

#### Nodule Growth Rate

We assume that within the datable interval the newly formed nodule layers contain a fixed amount of <sup>10</sup>Be which is not subjected to post-depositional migration. Then the slope of the plot of lnBe<sup>10</sup> concentration versus depth gives a measure of the nodule growth rate, according to the relationship:

TABLE 3

U, Th, Pa in ARIES 13D and Mn 139  
(on sample splits measured for Be)

Sample No.	Depth (mm)	U <sup>238</sup> (dpm/g)	Th <sup>232</sup> (dpm/g)	$\frac{U^{234}}{U^{238}}$ <sup>1</sup>	Th <sup>230</sup> <sub>ex</sub> (dpm/g)	Pa <sup>231</sup> <sub>ex</sub> (dpm/g)
<u>ARIES 13D</u>						
L1	0-4.3	9.19±.42	3.42±.17	0.97±.05	12.4±.8	4.55±.42
L2	4.3-8.8	9.30±.38	1.80±.14	0.99±.04	0.26±.54	-0.04±.03
L3	8.8-18.2	6.56±.25	0.75±.06	0.96±.04	0.18±.33	0.12±.08
<u>Mn 139</u>						
L1	0-0.8	8.62±.60	28.7±3.2	1.14±.10	388±12	22.1±1.9
L2	0.8-3.6	10.3±.44	18.4±2.3	0.96±.04	55.4±7.9	4.37±.30
L3	3.6-9.4	7.42±.44	11.0±.8	0.98±.06	10.3±.9	0.70±.10
L4	9.4-24.1	7.35±.34	8.81±.54	1.02±.06	4.62±.69	0.43±.15
L5	24.1-38.4	7.15±.43	7.94±.46	1.01±.07	1.13±.64	0.67±.23
Bo	59.1-65.0	8.94±.37	3.31±.22	1.06±.05	-0.47±.56	-0.03±.10
Su	< 1.0	7.67±.46	13.1±.9	1.03±.07	18.0±1.7	0.95±.14
S4	0- < 1.5 (irregular)	9.43±.57	4.55±.42	1.09±.07	6.10±1.34	3.73±.39

1. Activity ratio

2.  $Th_{ex}^{230} = \text{dpm/g}(Th^{230}) - \text{dpm/g}(U^{234})$ ;  $Pa_{ex}^{231} = \text{dpm/g}(Pa^{231}) - \text{dpm/g}(U^{235})$ .

$$\frac{d \ln C}{dz} = \frac{-\lambda}{S} \quad (1)$$

where  $C = \text{Be}^{10}$  concentration

$\lambda =$  decay constant of  $\text{Be}^{10}$

$S =$  growth rate

$z =$  space (depth) coordinate, origin fixed at nodule surface, positive axis into nodule.

Figures 3 and 4 show plots of the  $\text{Be}^{10}$  concentration data for ARIES 13D and Mn 139, respectively. Similar plots can be made using the  $\text{Be}^{10}/\text{Be}^9$  ratio or excess  $\text{Th}^{230}$  ( $\text{Th}_{\text{ex}}^{230}$ ) and  $\text{Pa}^{231}$  ( $\text{Pa}_{\text{ex}}^{231}$ ) concentrations. Because of the uniformity of  $\text{Be}^9$  in the two nodules, depth plots of the  $\text{Be}^{10}/\text{Be}^9$  ratio give essentially the same results as the  $\text{Be}^{10}$  concentration shown in Figs. 3 and 4. Figure 5 is the equation (1) plot of  $\text{Th}_{\text{ex}}^{230}$  and  $\text{Pa}_{\text{ex}}^{231}$  for Mn 139, based on the data of Table 4.

TABLE 4

U, Th and Pa Data in Top Layers of Mn 139

Sample No.	Depth (mm)	$\text{U}^{238}$ (dpm/g)	$\text{Th}^{232}$ (dpm/g)	$\frac{\text{U}^{234}}{\text{U}^{238}}$ <sup>1</sup>	$\text{Th}_{\text{ex}}^{230}$ <sup>2</sup> (dpm/g)	$\text{Pa}_{\text{ex}}^{231}$ <sup>2</sup> (dpm/g)
T1	0-0.3	9.11±.44	33.2±2.1	1.18±.07	2210±117	93.2±3.7
T2	0.3-1.2	8.29±.42	25.6±2.4	1.11±.06	270±25	6.25±.31
T3	1.2-2.5	7.60±.39	18.6±1.3	1.10±.06	18.2±1.9	0.49±.03
T4	2.5-3.8	7.24±.45	12.3±.7	1.03±.07	8.56±.99	-0.01±.02
T5	3.8-4.9	6.51±.32	10.6±.8	1.00±.06	-----	-0.01±.02
T6	4.0-7.0	6.09±.91	9.83±.45	0.95±.04	0.12±.09	0.06±.04

1. Activity ratio

2.  $\text{Th}_{\text{ex}}^{230} = \text{dpm/g}(\text{Th}^{230}) - \text{dpm/g}(\text{U}^{234})$ ;  $\text{Pa}_{\text{ex}}^{231} = \text{dpm/g}(\text{Pa}^{231}) - \text{dpm/g}(\text{U}^{235})$ .

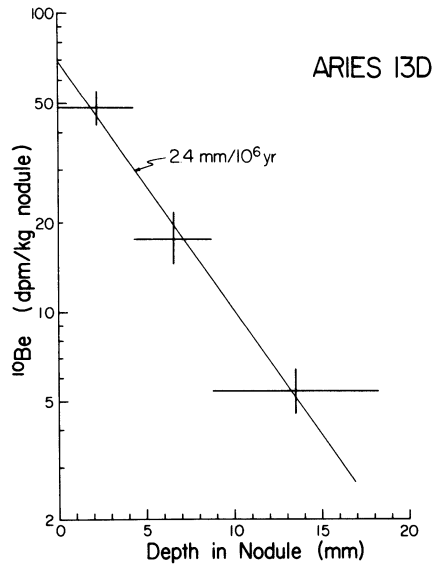


Fig. 3. Semilog depth plot of Be<sup>10</sup> in ARIES 13D. The slope of the best-fitting line gives an apparent growth rate of 2.4 mm/10<sup>6</sup>yr.

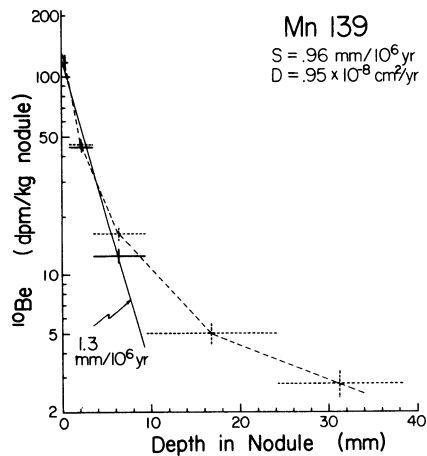


Fig. 4. Semilog depth plot of Be<sup>10</sup> in Mn 139. Measured data are shown by dashed lines. Correction for activities from side of the nodule (see text) yields a rate of 1.3 mm/10<sup>6</sup>yr (based on solid lines). The growth rate would be 0.96 mm/10<sup>6</sup>yr if Be<sup>10</sup> in nodule had an effective diffusion coefficient of 0.95 x 10<sup>-8</sup> cm<sup>2</sup>/yr.

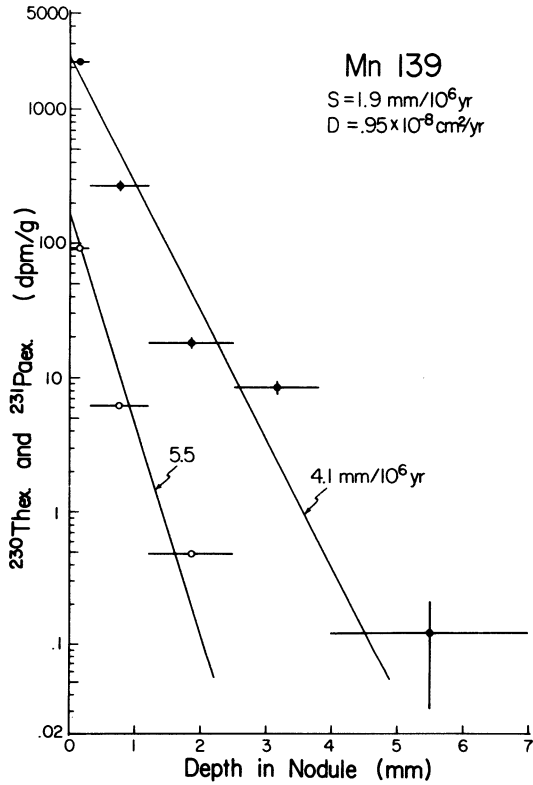


Fig. 5. Semilog depth plot of excess  $\text{Th}^{230}$  and  $\text{Pa}^{231}$  in Mn 139. The 5.5 and 4.1  $\text{mm}/10^6 \text{ yr}$  figures are estimates assuming no diffusion of the nuclides (equation (1) plots). Calculated effective diffusion coefficient for  $\text{Th}^{230}$  and  $\text{Pa}^{231}$  is  $0.95 \times 10^{-8} \text{ cm}^2/\text{yr}$ , which results in a growth rate of 1.9  $\text{mm}/10^6 \text{ yr}$ .

A growth rate of 2.4 mm/10<sup>6</sup>yr averaged over the top ~ 15 mm of ARIES 13D is obtained from Be<sup>10</sup> (Fig. 3). This information would predict absence of measurable Th<sub>ex</sub><sup>230</sup> and Pa<sub>ex</sub><sup>231</sup> in the deeper two layers of the nodule, L2 and L3. Data in Table 3 agree with this prediction.

Before examining the Be<sup>10</sup> results of Mn 139, it should be pointed out that the apparent increase in growth rate for the deeper layers, as indicated by the decrease in Be<sup>10</sup> gradient with depth (Fig. 4), could well be a sampling artifact. In peeling off different growth layers for analysis, the possibility exists that the scraped surfaces are not always parallel to the growth surfaces. This situation is likely to be more aggravated for deeper layers. Furthermore, in the present case where a large area has been scraped, we have overlooked the "bending" of the growth layers at the marginal part of the nodule specimen while sampling layers L1 through L5 (Figs. 1B and 6). The "bending" is a result of the concentric nature of accretion, leading to the effect that material on the side of Mn 139 can be much younger than that of the interior at the same "depth level" from top. This is evidenced by the amount of Be<sup>10</sup>, Th<sub>ex</sub><sup>230</sup>, and Pa<sub>ex</sub><sup>231</sup> in sample Si being significantly higher than the layers "above" (Tables 2 and 3; cf. Fig. 6). Contamination of younger material into deeper layers from the side could, therefore, cause the curvature in the Fig. 4 plot.

We can estimate the magnitude of the contamination. As Fig. 6 illustrates, the sampled area is approximated by a quadrant with a radius of 90 mm. Assuming that the thickness of growth layers remains the same on all sides of the nodule, we estimate that the % volumes (or weights) of nodule material contaminated into underlying layers are about 1.8% of L1, 6.0% of L2, 12% of L3, and 27% of L4. Based on these estimates and the measured Be<sup>10</sup> concentrations for each layer, corrections can be made of the contaminations. The corrected Be<sup>10</sup> values are listed in Table 5. In the same table are also presented the corrected values of excess Th<sup>230</sup> and excess Pa<sup>231</sup> obtained in the same manner as for Be<sup>10</sup>. The negative values assigned to layers L4 and L5 (Table 5) suggest that the corrections may be overly made so that the corrected Be<sup>10</sup> concentration gradient becomes an upper bound. However, as shown in Fig. 4, for the first 3 data points, the effect of corrections is minor.

Iterative least-squares fit to an exponential function (Wolberg, 1967) gives the following slope values (in cm<sup>-1</sup>) for Be<sup>10</sup>, Th<sub>ex</sub><sup>230</sup> and Pa<sub>ex</sub><sup>231</sup> in the plots of Figs. 4 and 5:

$$\left. \frac{d \ln C}{dz} \right|_{\text{Be}} = -3.58, \quad \left. \frac{d \ln C}{dz} \right|_{\text{Th}} = -22.5, \quad \left. \frac{d \ln C}{dz} \right|_{\text{Pa}} = -36.9.$$

From (1), the Be<sup>10</sup>-derived rate of growth for the top 10 mm of

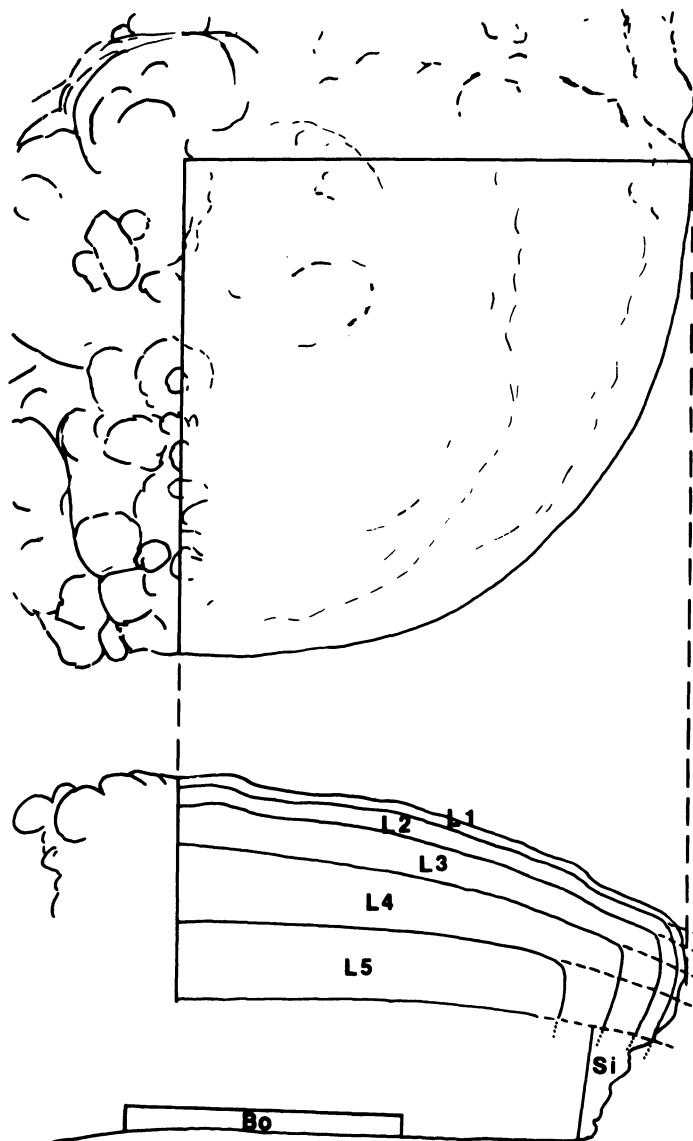


Fig. 6. Top is a plan view of part of Mn 139, showing the quadrant-shaped sampled area. The side view (bottom) shows that the boundaries of the sampled layers are assumed to follow those of the growth layers, except near the margin where the latter could be "bended" around (cf. Fig. 1B). Extent of contamination of material from upper to lower layers, as given in the text, is estimated assuming that the thickness of growth layer remains nearly constant around the nodule.

Mn 139 is 1.3 mm/10<sup>6</sup>yr. This compares with the Th<sub>ex</sub><sup>230</sup>-based rate of 4.1 mm/10<sup>6</sup>yr and Pa<sub>ex</sub><sup>231</sup>-based rate of 5.5 mm/10<sup>6</sup>yr. Although these values have uncertainties of at least ±20% and are averages over different depth ranges (hence time scales), a three- to four-fold increase in the Th<sup>230</sup> and Pa<sup>231</sup> rates in relation to the Be<sup>10</sup> rate merits discussion.

TABLE 5

Corrected Be<sup>10</sup>, Th<sub>ex</sub><sup>230</sup> and Pa<sub>ex</sub><sup>231</sup> in Layers L1-L5 of Mn 139

Layer	z* Contamination	Corrected Be <sup>10</sup> (dpm/kg)	Corrected Th <sub>ex</sub> <sup>230</sup> (dpm/g)	Corrected Pa <sub>ex</sub> <sup>231</sup> (dpm/g)
L1	0	118±11	388±12	22.1±1.9
L2	1.8	44.9±3.1	49.3±7.9	4.05±.30
L3	7.8	12.6±1.4	0.39±.9	0.064±.10
L4	19.8	-1.60±.61	-6.76±.69	-0.27±.15
L5	46.8	-5.87±.45	-13.3±.64	0.12±.23

\* L2 is assumed to be contaminated by 1.8% (L1), L3 by 1.8% (L1) + 6.0% (L2), etc.

It is possible that the Pa<sup>231</sup> as well as the Th<sup>230</sup> rates are too high. This stems from the consideration that any homogenization processes such as diffusion and mixing (due largely to sampling on crenulated growth surfaces) would tend to reduce the concentration gradients of shorter-lived radioisotopes more than those of longer-lived ones. To a first approximation, the true growth rate could be close to the 1.3 mm/10<sup>6</sup>yr figure depicted by Be<sup>10</sup> decay.

If diffusion-mixing does occur, its effect on growth rate estimates from equation (1) can be evaluated as the following.

### Diffusion-Decay Model

It is assumed that any mixing or transport mechanism for radio-nuclides in Mn 139 along its growth direction is likened to a diffusional process, characterized by a constant "effective" diffusion coefficient. The steady state distribution of the nuclide as a function of depth (normal to growth surface) in the nodule can be written as:

$$D \frac{d^2C}{dz^2} - S \frac{dC}{dz} - \lambda C = 0 \quad (2)$$

where  $D$  = effective diffusion coefficient ( $\text{cm}^2\text{yr}^{-1}$ )

$C$  = concentration ( $\text{dpm cm}^{-3}$ )

$\lambda$  = decay constant ( $\text{yr}^{-1}$ )

$S$  = growth rate ( $\text{cm yr}^{-1}$ )

$z$  = depth in nodule, origin at top surface, positive downward (cm).

For the boundary conditions:  $C = C_0$  at  $z = 0$ ,  $C = 0$  at  $z = \infty$ , the solution is:

$$C = C_0 e^{Az} \quad (3)$$

$$\text{where } A = \frac{S}{2D} - \left( \frac{S^2}{4D^2} + \frac{\lambda}{D} \right)^{1/2} \quad (4)$$

Note  $A = \frac{d \ln C}{dz}$ ; its numerical values for  $\text{Be}^{10}$ ,  $\text{Th}^{230}$  and  $\text{Pa}^{231}$  in Mn 139 have been given earlier.

To estimate the magnitude of  $S$  and  $D$ , we proceed with two approaches. First, taking the aforementioned approximation of  $S = 1.3 \text{ mm}/10^6\text{yr}$  and applying it to the intervals measured for  $\text{Th}^{230}$  and  $\text{Pa}^{231}$ , we obtain from equation (4)  $D$  values of  $1.2 \times 10^{-8} \text{ cm}^2/\text{yr}$  and  $1.1 \times 10^{-8} \text{ cm}^2/\text{yr}$  for  $\text{Th}^{230}$  and  $\text{Pa}^{231}$  respectively. Another approach is to suppose that the data for  $\text{Th}^{230}$  and  $\text{Pa}^{231}$  would yield common  $S$  and  $D$ , in view of the two nuclides' rather similar geochemical behavior and applicable depth range. Therefore, with  $A$  values known for  $\text{Th}^{230}$  and  $\text{Pa}^{231}$ , we solve equation (4) simultaneously for  $S$  and  $D$ :  $S = 1.9 \text{ mm}/10^6\text{yr}$  and  $D = 0.95 \times 10^{-8} \text{ cm}^2/\text{yr}$ . Assuming  $\text{Be}^{10}$  to have a similar  $D$  of  $0.95 \times 10^{-8} \text{ cm}^2/\text{yr}$ , then the  $\text{Be}^{10}$ -based growth rate would be reduced from 1.3 to 0.96  $\text{mm}/10^6\text{yr}$ .

The model calculations thus show that, because of the slow growth nature of nodules, diffusion-mixing transport of radio-isotopes, if occurring, could significantly affect growth rate determination. As expected, given the same effective diffusivity, the shorter-lived isotopes would be more vulnerable to giving high apparent rates than the longer-lived ones. In the present case, with a  $D$  value of  $\sim 10^{-8} \text{ cm}^2/\text{yr}$ , the  $\text{Th}^{230}$ -based and  $\text{Pa}^{231}$ -based apparent rates obtained for the surface 2.5-5 mm of Mn 139 are shown to be too large by about 2 to 3 times. The same  $D$  applied

to Be<sup>10</sup> would result in an apparent rate about 30% too high (cf. Figs. 4 and 5).

#### Amounts of Be<sup>10</sup>, Th<sup>230</sup>, and Pa<sup>231</sup> in Nodules

Ku and Broecker (1969) first pointed out that only a fraction of Th<sup>230</sup> and Pa<sup>231</sup> produced in the water column entered manganese nodules. Bhat et al. (1973) showed the same for Be<sup>10</sup>. These observations are also indicated by the present data. Let  $p$  be the production rate, and  $C$ ,  $z$ , and  $\lambda$  as defined before, the fraction of radionuclides incorporated in nodule is:

$$f = \frac{\lambda}{p} \left[ \int_0^{\infty} C(z) dz \right] \quad (5)$$

Taking a water depth of 3430 m, a uranium concentration of 3.3  $\mu\text{g/l}$  and  $\text{U}^{234}/\text{U}^{238} = 1.14$ , we estimated at the sampling sites of ARIES 13D and Mn 139 the production rates (in  $\text{dpm cm}^{-2} \text{yr}^{-1}$ ) of Th<sup>230</sup> and Pa<sup>231</sup> to be:  $p(\text{Th}^{230}) = 8.77 \times 10^{-3}$  and  $p(\text{Pa}^{231}) = 7.73 \times 10^{-4}$ . The production rate of Be<sup>10</sup> is about  $4.7 \times 10^{-7} \text{ dpm cm}^{-2} \text{yr}^{-1}$  (Amin et al., 1975).

Values of  $f$  in the two nodules are thus calculated from (5) as:

ARIES 13D:  $f_{\text{Be}} = 0.07$ ,  $f_{\text{Th}} = 0.01$ ,  $f_{\text{Pa}} = 0.10$ ; (assuming no activities on the bottom side).

Mn 139:  $f_{\text{Be}} = 0.06$ ,  $f_{\text{Th}} = 0.20$ ,  $f_{\text{Pa}} = 0.18$ .

One notes that these values are generally small and highly variable. Published data tend to reinforce this notion (Ku and Broecker, 1969; Krishnaswami, et al., 1972). The variability may occur even in a single specimen. As in the case of Mn 139, the depth integrated Be<sup>10</sup>, Th<sup>230</sup>, and Pa<sup>231</sup> in the "smooth" half of the nodule appear to be much more than those in the "knobby" half (Fig. 1B). This refers to the data of sample L1 versus sample Su (Tables 3 and 5). Even in the smooth half,  $\Sigma\text{Th}^{230}$  under Area T (Fig. 1) is more than that under Area L (Tables 4 and 5). It is tempting to suggest the variation as being due to the sediment veneer on nodule surface often revealed by the bottom photographs. Knobby surfaces tend to trap sediment particles more readily which then shield the nodule from isotopes scavenged from above. That the parameter  $f$  reflects the fraction of a nodule's lifetime uncovered by sediments (Bhat et al., 1973) is a plausible proposition. In a sense, the process of nodule growth is not a continuous one.

#### An Evaluation of the Concept of "Exposure-Diffusion"

It has been hypothesized (Arrhenius, 1967; Lalou and Brichet, 1972) that nodules could form very rapidly without inclusion of any unsupported Th<sup>230</sup>. After formation they receive the rain of radionuclides but experience almost no growth on the

sea floor. The observed rapid decrease with depth of the nuclides could result from inward diffusion-mixing processes. Accordingly, the age of the nodule can be derived from the observed integrated amount of a nuclide, knowing its production rate. That is, the length of time during which nodules are "exposed" to the radioactivity flux is calculated from (with notations defined as above):

$$t = -\frac{1}{\lambda} \ln \left[ 1 - \frac{\lambda}{P} \left( \int_0^{\infty} C dz \right) \right] \quad (6)$$

Or from equation (5):

$$t = -\frac{1}{\lambda} \ln(1-f) \quad (7)$$

This "exposure-diffusion" hypothesis has several serious flaws as viewed from the radiochemical consequences it entails.

(1) Commonly observed values for  $f$  are small; this leads to much younger ages for the nodules than implied in our previous discussion. The "exposure" ages of Mn 139 are calculated to be 127,000 yr, 24,200 yr, and 9,800 yr, based on the observed  $f$ 's for Be<sup>10</sup>, Th<sup>230</sup>, and Pa<sup>231</sup> respectively. For ARIES 13D, the disparity in these ages is even larger, and it remains to be explained.

(2) Implicit in the age calculation is the assumption that nodules collect with 100% efficiency the Be<sup>10</sup>, Th<sup>230</sup> and Pa<sup>231</sup> produced above them, on a unit area basis. The fact that, due to their reactivity, a significant portion of these nuclides could be scavenged by particulate phases into the adjacent sediments rather than incorporated into nodules, puts strain on this assumption.

(3) As has been pointed out (Ku, 1977), the absence of deficiencies of Th<sup>230</sup> and Pa<sup>231</sup> relative to their uranium parents in the inner parts of both nodules studied is unexpected in view of the young "exposure" ages and the rapid formation requirement.

(4) Recent works (Ku *et al.* 1975; Ku and Knauss, 1978) have shown that the internal fractures of manganese nodules may contain filling material > 300,000 years old. Clearly, this age cannot be reconciled with the young exposure ages.

(5) Given the assumptions required by the exposure-diffusion (with no growth) concept, one can model as follows the distribution of radionuclides in a nodule, giving further insight into the reality of the concept.

Exposure-diffusion model. The concept can be approximated by considering the Fick's second-law equation (radio-decay is omitted owing to  $t \ll \lambda^{-1}$ ):

$$\frac{\partial C}{\partial t} = D \frac{\partial^2 C}{\partial z^2} \quad (8)$$

The initial condition is  $t=0, C=0$ . The upper boundary

receives a constant flux of radionuclides (with hardly any volume) equivalent to their production rates,  $p$ , namely:

$$t > 0, p = -D \left. \frac{\partial C}{\partial z} \right|_{z=0} = \text{constant. At the lower boundary: } z \rightarrow \infty, C \rightarrow 0.$$

The solution can be found in Carslaw and Jaeger (1959, p. 75) and in Duursma and Hoede (1967):

$$C(z,t) = \frac{2p}{D} \left[ \left( \frac{Dt}{\pi} \right)^{1/2} \exp\left(-\frac{z^2}{4Dt}\right) - \frac{z}{2} \operatorname{erfc} \frac{z}{2(Dt)^{1/2}} \right] \quad (9)$$

In the first place, we see that, according to the model,  $\ln C$  varies with  $z^2$ , rather than with  $z$  as depicted by equations (1) and (3). Also, the dependency of  $C$  on  $z$  is rather strong due to the error function. This results in the convex-upward curvature in the  $\ln C$  vs.  $z$  plots of equation (9), as shown in Figs. 7 and 8 for the cases of Be<sup>10</sup> and Th<sup>230</sup> in Mn 139. In these figures, using the exposure ages ( $t$ ) and the  $P$  values given earlier,  $C(z)$  is plotted for different  $D$ 's.

The upward convexity in the depth plot of  $\ln C$  have rarely been observed. In fact, measured profiles not uncommonly show opposite (concave-upward) curvature, such as the cases in Figs. 7 and 8. This cannot always be the result of sampling artifact, since the Be<sup>10</sup> data of Fig. 7 have already been somewhat overly corrected for this effect, and since such concave characteristics have also been exhibited by alpha-track profiles (e.g., Lalou et al., 1978).

#### Magnitude of Parameter D

The effective diffusion coefficients computed from the diffusion-decay model for Mn 139 are of the order of  $10^{-8}$  cm<sup>2</sup>/yr. Values significantly higher than this, in effect, are not allowed by the model. This is seen from (4):

$$S = AD - \lambda/A \quad (10)$$

Since  $S$  must be  $> 0$  and  $A < 0$ , it follows:

$$D < \lambda/A^2 \quad (11)$$

For Mn 139, equation (11) depicts that  $D_{Be} < 3.6 \times 10^{-8}$  cm<sup>2</sup>/yr,  $D_{Th} < 1.8 \times 10^{-8}$  cm<sup>2</sup>/yr and  $D_{Pa} < 1.5 \times 10^{-8}$  cm<sup>2</sup>/yr.

From Figs. 7 and 8, the best  $D$  values according to the exposure-diffusion model are of the order of  $5 \times 10^{-7}$  cm<sup>2</sup>/yr, although the curve fitting for the model is far from ideal. In these cases, smaller  $D$  values such as  $10^{-8}$  cm<sup>2</sup>/yr depicted by the diffusion-decay model are clearly not permissible. One might thus suggest that an evaluation of  $D$  for Th<sup>230</sup> and Pa<sup>231</sup> in nodules would be useful to further appraise the two models.

The parameter  $D$  could characterize: (1) solid-state diffusion, (2) diffusion through the nodule pore water in the presence of instantaneous exchange with the solid, (3) physical mixing (in

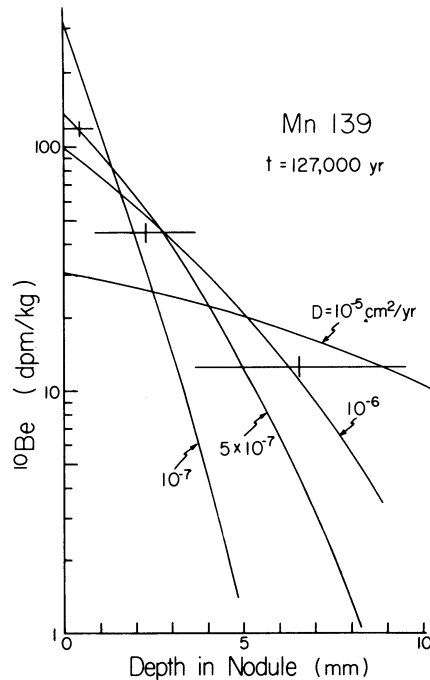


Fig. 7. Curves representing the  $\text{Be}^{10}$  distribution in Mn 139 as a function of  $D$ , as predicted by the "exposure-diffusion" model. Measured data points are shown for comparison.

situ, or artifact of sampling), or (4) combination of all three. Krishnaswami and Cochran (1978) pointed out that pure solid-state diffusion is possible but unlikely. These workers discussed the  $\text{Ra}^{226}$  distribution in nodules in terms of diffusion of  $\text{Ra}^{226}$  through nodule pore water. They obtained a model diffusion coefficient  $D_{\text{Ra}} \approx 10^{-6} \text{ cm}^2/\text{yr}$ , and attributed this low value (compared to  $\sim 10^2 \text{ cm}^2/\text{yr}$  for molecular diffusivity,  $D_m$ , in free solution: Li and Gregory, 1974) to rapid equilibrium adsorption of  $\text{Ra}^{226}$  on solids and the high tortuosity of diffusion paths in the nodule. This arises from the relationship:

$$D \approx D_m / (\theta^2 \cdot K) \quad (12)$$

where  $\theta^2$  denotes tortuosity and  $K$  the ion exchange or adsorption equilibrium constant ( $= C_{\text{nodule}}/C_{\text{pore water}}$ ). The value of  $K$  for  $\text{Ra}^{226}$  was given as  $\sim 10^5$  (Krishnaswami and Cochran, 1978). The activity ratio of  $\text{Th}^{230}$  to  $\text{Ra}^{226}$  in nodules is close to unity, whereas that in the pore water, taken to be similar to that of

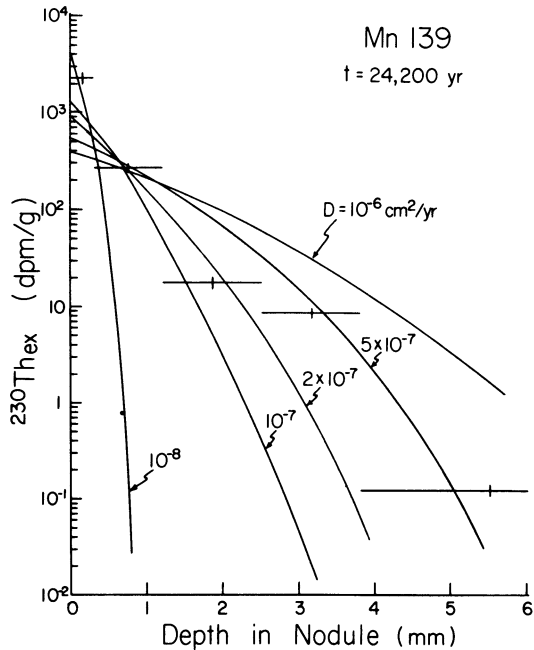


Fig. 8. Comparison of measured and predicted excess  $\text{Th}^{230}$  distribution in Mn 139. The predicted distribution, calculated for different  $D$  values, is from the "exposure-diffusion" model of equations (8) and (9).

bottom water, is about 0.01 - 0.05 (e.g., Ku, 1972). Therefore,  $K$  for  $\text{Th}^{230}$  should be  $(0.2-1) \times 10^7$ . Since  $D_m(\text{Th}) \approx 0.2D_m(\text{Ra})$  (Li and Gregory, 1974), from (12) we calculate:

$$D_{\text{Th}} \approx \frac{D_m(\text{Th})/(\theta^2 \cdot 10^7)}{D_m(\text{Ra})/(\theta^2 \cdot 10^5)} \times D_{\text{Ra}} \approx (0.2-1) \times 10^{-8} \text{ cm}^2/\text{yr} \quad (13)$$

In view of the strong chemisorption property of  $\text{Pa}^{231}$ , we expect that  $D_{\text{Pa}} < D_{\text{Th}}$ . Hence, the  $D$  values of  $\sim 10^{-8} \text{ cm}^2/\text{yr}$  deduced earlier from the diffusion-decay model appear to be quite acceptable to our limited evidence about the possible magnitude of  $D$ .

Apparently, the extent of physical mixing must be small (as constrained by the rather small  $D$  values) in order for the diffusion-decay model to be applicable. Such could well be generally the case under careful sampling conditions, as shown by the  $\text{Pb}^{210}$  measurements of Krishnaswami and Cochran (1978).

### Summary

Various radioactivities--Th<sup>230</sup>, Pa<sup>231</sup>, Be<sup>10</sup>, Al<sup>26</sup>--present within the Mn-Fe oxide layers provide the most direct and useful clues to the ages of manganese nodules. A long established observation is their logarithmic decrease with depth in nodules. The decrease is such that it is more gradual for the longer-lived radionuclides than for the shorter-lived ones. The gradients, taken to reflect radioactive decay, generally yield concordant (to within error limits) growth-rate estimates of mm's/10<sup>6</sup>yr for the nodules.

A question arises as to what extent the gradients could be affected by processes other than radiodecay, i.e., by diffusion and/or diffusion-like mixing. A manifestation of these latter processes would be the apparent discordant rates based on Be<sup>10</sup>, Th<sup>230</sup>, and Pa<sup>231</sup>, such as found in Mn 139. Quantitative evaluation using a diffusion-decay model shows that the apparent discordancy can be explained by mixing processes characterized by "effective" diffusion coefficients of the order of 10<sup>-8</sup> cm<sup>2</sup>/yr. The true growth rate, obviously, would be slower than the apparent rates.

The depth integrated dpm/cm<sup>2</sup> of Be<sup>10</sup>, excess Th<sup>230</sup> and excess Pa<sup>231</sup> in nodules in general is variable and small in amount, compared to their potential source of supply and their inventory in sediments. In Mn 139 the variability occurs even in different parts of its upper surface. The observations are best explained by the suggestion that on a unit area basis nodules receive a small share of the isotopes relative to that received by other sedimentary phases.

Critiques of the proposed catastrophic formation and young "exposure" ages for nodules are presented. Mathematical modeling of such concept of nodule formation leads to depth distribution of the radioisotopes rather different from the simple exponential form that is commonly observed.

### Acknowledgments

D. Z. Piper and J. L. Bischoff of the U. S. Geological Survey and T. Walsh of the Scripps Institution of Oceanography (SIO) kindly provided the nodule specimens from collections of their respective institutions. We are indebted to F. Guichard of Centre des Faibles Radioactivites for his knowledge in Be<sup>10</sup> analytical chemistry, to Y. C. Chung of SIO for providing the beta counting standards, and to A. Sycip of the U.S.C. Environmental Engineering Program for assistance in the Be<sup>9</sup> measurements. Mr. S. Y. Meng ably aided in the U-series isotope analyses.

Financial support from the National Science Foundation through grant OCE77-04061 administered by the Seabed Assessment

Program of I.D.O.E. is gratefully acknowledged.

This is contribution #385 from the Department of Geological Sciences, University of Southern California.

### References

- Amin, B. S., Lal, D. and Somayajulu, B. L. K. (1975) Chronology of marine sediments using the Be<sup>10</sup> method: intercomparison with other methods. Geochim. Cosmochim. Acta 39, 1187-1192.
- Arrhenius, G. (1967) Deep-sea sedimentation: a critical review of U.S. work. Trans. Am. Geophys. Union, 48, 604-631.
- Bender, M. L., Ku, T. L. and Broecker, W. S. (1966) Manganese nodules: Their evolution. Science 151, 325-328.
- Bhat, S. G., Krishnaswami, S., Lal, D., Rama and Somayajulu, B. L. K. (1973) Radiometric and trace elemental studies of ferromanganese nodules. Proc. Symp. Hydrogeochem. Biogeochem., I, 443-462, Clarke, Washington, D.C.
- Carslaw, H. S. and Jaeger, J. C. (1959) Conduction of Heat in Solids (2nd edition) Oxford Univ. Press.
- Duursma, E. K., and Hodge, C. (1967) Theoretical, experimental and field studies concerning molecular diffusion of radioisotopes in sediments and suspended solid particles of the sea, Part A: theoretical and mathematical calculation. Netherland Jour. Sea Res. 3, 423-457.
- Guichard, F., Reyss, J. L. and Yokoyama, Y. (1978) Growth rates of manganese nodules measured with <sup>10</sup>Be and <sup>26</sup>Al. Nature 272, 155-156.
- Krishnaswami, S. and Cochran, J. K. (1978) Uranium and thorium series nuclides in oriented ferromanganese nodules: growth rates, turnover times and nuclide behavior. Earth Planet. Sci. Lett. 40, 45-62.
- Krishnaswami, S., Somayajulu, B. L. K. and Moore, W. S. (1972) Dating of manganese nodules using beryllium-10. In Papers from a Conference on Ferromanganese Deposits on the Ocean Floor (ed. D. R. Horn) 117-122. NSF, Washington, D.C.
- Ku, T. L. (1972) Radium in the ocean. In Encyclopedia of Geochemistry and Environmental Sciences (ed. R. W. Fairbridge), 1008-1014, Van Nostrand Reinhold, N.Y.
- Ku, T. L. (1977) Rates of accretion. In Marine Manganese Deposits (ed. G. P. Glasby) 249-267, Elsevier, N.Y.
- Ku, T. L. and Broecker, W. S. (1969) Radiochemical studies on manganese nodules of deep-sea origin. Deep-Sea Res. 16, 625-637.
- Ku, T. L. and Knauss, K. G. (1978) Radiocative disequilibrium in fissure-filling material and its implication in dating of manganese nodules. Colloque International du C.N.R.S. No. 289 sur la Genèse des Nodules de Manganèse, Gif-sur-Yvette, 25-30 September.

- Ku, T. L., Knauss, K. G. and Lin, M. C. (1975) An evaluation of dating nodules by the uranium series isotopes. EoS, Trans. Am. Geophys. Un. 56, 999.
- Lal, D. and Schink, D. R. (1960) Low background thin-wall flow counters for measuring the beta activity of solids. Rev. Sci. Instr. 31, 395-398.
- Lalou, C. and Brichet, E. (1972) Signification des mesures radiochimiques dans l'évaluation de la vitesse de croissance des nodules de manganèse. C. R. Acad. Sc. Paris. Série D, 275, 815-818.
- Lalou, C., Ku, T. L., Brichet, E., Poupeau, G. and Romary, P. (1978) TECHNO encrustation I: radiometric studies. Colloque International du C.N.R.S. No. 289 sur la Genèse des Nodules de Manganèse, Gif-sur-Yvette, 25-30 September.
- Li, Y. H. and Gregory, S. (1974) Diffusion of ions in sea water and in deep-sea sediments. Geochim. Cosmochim. Acta 38, 703-714.
- Wolberg, J. R. (1967) Prediction Analysis. Van Nostrand, Princeton, New Jersey.